



OPEN

The superior photocatalytic performance and DFT insights of S-scheme CuO@TiO₂ heterojunction composites for simultaneous degradation of organics

Hesham Hamad^{1✉}, Mohamed M. Elsenety², Wagih Sadik³, Abdel-Ghaffar El-Demerdash³, Adel Nashed³, Amr Mostafa³ & Shaimaa Elyamny⁴

The necessity to resolve the issue of rapid charge carrier recombination for boosting photocatalytic performance is a vigorous and challenging research field. To address this, the construction of a binary system of step-scheme (S-scheme) CuO@TiO₂ heterostructure composite has been demonstrated through a facile solid-state route. The remarkably enhanced photocatalytic performance of CuO@TiO₂, compared with single TiO₂, which can consequence in the more efficient separation of photoinduced charge carriers, reduced the band gap of TiO₂, improved the electrical transport performance, and improved the lifetimes, thus donating it with the much more powerful oxidation and reduction capability. A photocatalytic mechanism was proposed to explain the boosted photocatalytic performance of CuO@TiO₂ on a complete analysis of physicochemical, DFT calculations, and electrochemical properties. In addition, this work focused on the investigation of the stability and recyclability of CuO@TiO₂ in terms of efficiency and its physical origin using XRD, BET, and XPS. It is found that the removal efficiency diminishes 4.5% upon five recycling runs. The current study not only promoted our knowledge of the binary system of S-scheme CuO@TiO₂ heterojunction composite photocatalyst but also shed new light on the design of heterostructure photocatalysts with high-performance and high stability.

Recently, the developments of demand for fabrication of new semiconductors with various characteristics have been grown by the dynamic progress of the chemical industry. TiO₂ has gotten a lot of interest in photocatalysis because of its strong oxidizing capability, long-term photostability and lack of toxicity^{1,2}. However, the traditional photocatalysis using TiO₂ is restricted by various factors including the fast recombination of photogenerated electron (e⁻) and holes (h⁺), low absorption of solar light, and low photocatalytic activity on the conventional crystal facets, which meaningfully hinders the practical application till now, this problem is unsolved^{3,4}. So, the formation of heterojunction donates the highly efficient separation of photo-generated e⁻/h⁺ pairs by modification of TiO₂ surface with other semiconductors can be an active strategy to boost the efficiency of photocatalysis process⁵.

Copper oxides have a narrow band gap and are a p-type semiconductor. Cupric oxide (CuO) and cuprous oxide (Cu₂O) are the two types of crystals of copper oxides⁶. CuO is a monoclinic phase, whereas Cu₂O has a cubic structure, which CuO is more thermostable than Cu₂O⁷. As a sensitizer of TiO₂, CuO is an appealing substance. As a result, the heterojunction between n-TiO₂ and p-CuO is mainly promising in this regard, as it

¹Fabrication Technology Research Department, Advanced Technology and New Materials Research Institute (ATNMRI), City of Scientific Research and Technological Applications (SRTA-City), New Borg El-Arab City, Alexandria 21934, Egypt. ²Department of Chemistry, Faculty of Science, Al-Azhar University, P.O. 11823, Nasr City, Cairo, Egypt. ³Materials Science Department, Institute of Graduate Studies and Research (IGSR), Alexandria University, Alexandria, Egypt. ⁴Electronic Materials Research Department, Advanced Technology and New Materials Research Institute, City of Scientific Research and Technological Applications (SRTA-City), P.O. Box 21934, New Borg El-Arab City, Alexandria, Egypt. ✉email: hhamad@srtacity.sci.eg

enables the separation and transit of photo-induced charge carriers in CuO@TiO₂, and subsequently minimizes the possibility of recombination and increases the photocatalytic capabilities⁸. Due to the formation of CuO–TiO₂ p–n heterojunction, the photo generated holes migrate towards the interface, whereas the electrons migrate towards the bulk. As a result, the p–n junction is predictable in terms of charge carrier production and lifetime, which has a positive impact on the photocatalytic performance^{9,10}.

Recently, a step (S)-scheme heterojunction photocatalysts with spatially separated reduction and oxidation units is hot topic because the photoinduced electrons and holes accumulate in the semiconductor with the more negative conduction band (CB) position and the other semiconductor with the more positive valence band (VB) position, respectively, in the recently. Such a novel heterojunction ensures visible light absorption, enhanced charge separation, and higher charge carrier redox capacity all at the same time. Aside from the two semiconductors' matching band structures, an intimate interfacial contact between them is critical for promoting the S-scheme charge transfer path across the interface^{11,12}.

Based on the above research background and assumptions, to date, no study has been focused on the photocatalytic application of a binary system of S-scheme CuO@TiO₂ heterojunction nanocomposite. Herein, the goal of this research was the demonstration of facile solid-state synthesis of a binary system of S-scheme CuO@TiO₂ heterojunction nanocomposite which was built by surface modification of TiO₂ by CuO. The heterojunction formed between TiO₂ and CuO induces the efficient separation of photogenerated e⁻/h⁺. We found that the surface modification strongly influences the properties of the produced photocatalyst (structure, composition, etc.) that are characterized by various physicochemical techniques and correlated with the photocatalytic performance of the samples. The enhancement of photocatalytic activity was proposed and explained in detail according to the mechanism of e⁻/h⁺ separation. In this inquiry, two crucial properties of CuO@TiO₂, namely stability, and reusability, were also examined, particularly in terms of industrial-scale application.

Results and discussions

Structural analysis. The structural characteristics of pure CuO and pure TiO₂ powder were characterized as the contrasts to binary CuO@TiO₂ heterostructure nanocomposites that shown in Fig. 1a. The diffraction peaks at scattering angles (2θ) of 32.0, 35.95°, 38.21° and 48.34° were indexed to (1 1 0) (– 1 – 1 1), (1 1 1), and (2 0 2) planes of monoclinic structure of CuO, respectively, which corresponding to JCPDS No. 48-1548¹³. Furthermore, the P-25 consists of anatase and rutile phases, matching very well with the confirmation of JCPDS No. 021-1272 and 021-1276, respectively¹⁴. Pure TiO₂ and CuO peaks exhibit the high intensity and sharp nature, indicating pure crystalline nature. Other phases, such as impurities, Cu₂O or metallic Cu, are not present, indicating that pure CuO could be achieved by chemical and calcination methods. The findings show that the binary composite of CuO@TiO₂ heterostructures contains two-phase TiO₂ and CuO compositions after the solid state reaction. CuO@TiO₂ heterostructure nanocomposites show more XRD peaks than TiO₂, indicating that CuO is present on the surface of the TiO₂¹⁵. The higher intensity of (– 1 – 1 1) and (111) diffraction peaks in CuO@TiO₂, could be due to the shield effect from the CuO nanoparticles¹⁶. However, a small gradual shift of the characteristic peak (101) of TiO₂ is observed towards a lower 2θ value after the formation of CuO@TiO₂, which could be attributed to partial substitution of titanium atom (ionic radius Ti⁴⁺, 0.074 nm) by the larger size of Cu atom (ionic radius Cu²⁺, 0.087 nm) at surface interaction^{17,18}, as we suggested and studied by DFT calculations. The same phenomena were studied and confirmed due substitution of I atom by another halogen of Br and Cl atoms in lead-free perovskites¹⁹.

Moreover, it is vital to note that Raman spectroscopy is a surface-probing technique, whereas XRD samples analyze the bulk. As a result, Raman spectra revealed a surface modification caused by the vibrational mode. Figure 1b illustrates the Raman spectra of TiO₂, CuO and its binary composite CuO@TiO₂ heterostructure. In the Raman spectrum of TiO₂, the active vibrational modes are recognized as: (i) the symmetric vibration of O–Ti–O in TiO₂ due to the doubly E_g modes at 145 and 606 cm⁻¹; and (ii) the symmetric bending vibration of O–Ti–O due to the B_{1g} modes at 437 cm⁻¹, while the A_g peak at 272 cm⁻¹ mode of CuO crystals, endorses the anatase-TiO₂ phase's distinctive peaks as reported in the literature^{20,21}. After solid state reaction, the modification by CuO affected on the position of the Raman peaks associated with the B_{1g} and A_{1g} vibration modes and confirmed the structural phases of TiO₂ and CuO for binary CuO@TiO₂ heterostructure as shown in Fig. 1b. Additionally, there is a blue shift at 404 cm⁻¹ which established the robust interaction obtainable in CuO@TiO₂. Cu²⁺ has a lower valence than Ti⁴⁺, therefore oxygen vacancies and other crystalline defects generated at the surface of TiO₂ by CuO helped to explain the spectrum behavior^{22,23}. The structural and vibrational features of the TiO₂ lattice were altered when CuO was added, demonstrating that CuO and TiO₂ had a strong interaction between them²⁴. Surface defects like this could act as photoactive centers, improving the charge separation efficiency²³.

Microstructure and elemental distribution. The microstructure of CuO and its binary system of CuO@TiO₂ heterostructure using SEM is shown in Fig. 2. Figure 2a provides an overview of the morphology of the CuO NPs which exhibit aggregated nanoparticles associated with irregular shape. In Fig. 2b, after solid state reaction, it revealed that the aggregated and interlinked nanocrystals, that aid in the intraparticle charge transfer. CuO nanoparticles also existed on the surface of TiO₂ nanoparticles.

The detailed morphology and microstructure of binary CuO@TiO₂ heterostructure nanocomposite were further investigated by high resolution transmission electron microscope (HR-TEM) and energy-dispersive X-ray spectroscopy (EDS). The corresponding HR-TEM image of CuO@TiO₂ heterostructure with different magnifications is presented at Fig. 2c–g. It is found that the extremely aggregated with irregularly shaped nanoparticles. The light gray regions are the TiO₂ microstructure, and the dark regions are CuO nanoparticles. This proved that the binary system of CuO@TiO₂ nanocomposite was crystalline in a uniform shape (not a physical mixture), but had the decoration of CuO on TiO₂ which formed the interface that leads to the CuO@TiO₂ heterojunction.

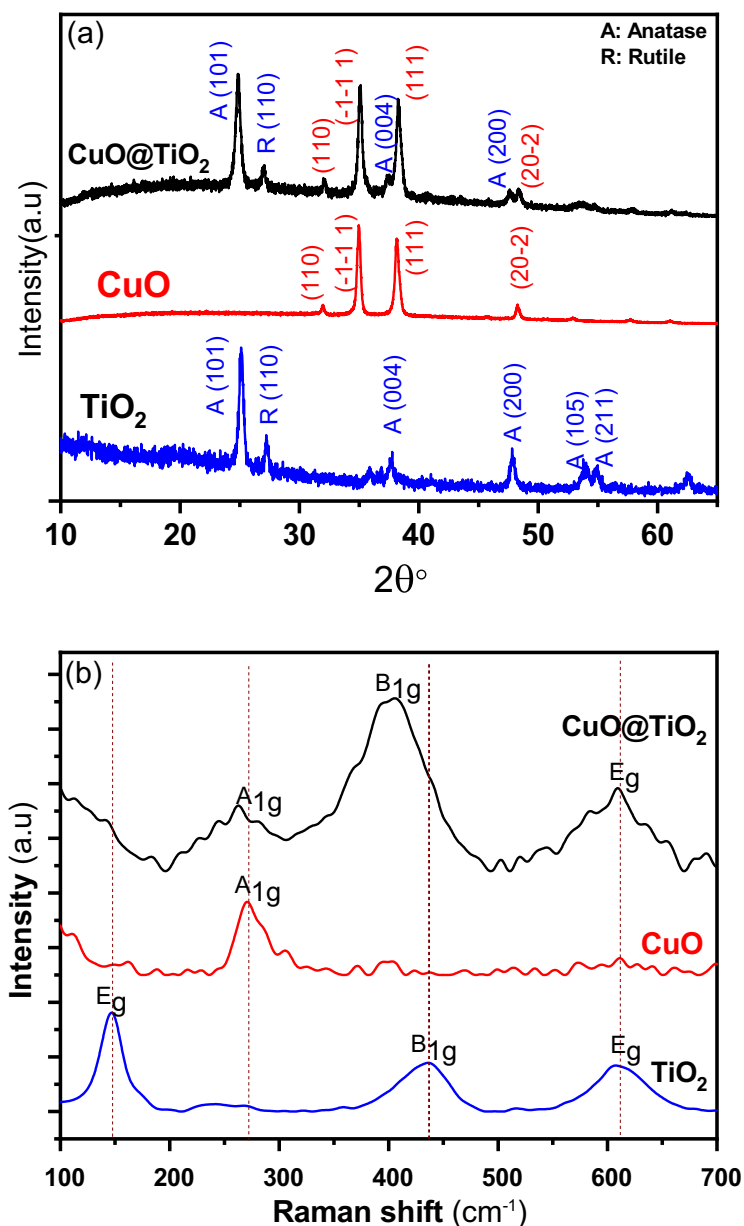


Figure 1. (a) XRD and (b) Raman spectra of TiO_2 , CuO , and its binary CuO@TiO_2 heterojunction nanocomposites.

Furthermore, it is well understood that having a large number of homogenous nanopores is favorable because it allows for the quick transfer of light-excited carriers to the particle surface, substantially lowering the carrier recombination rate and speeding up the photocatalytic reactions²⁵. The d-spacing value of TiO_2 was for the (101) and (110) crystal facets of TiO_2 had d-spacing values of 3.52 and 3.22 Å, respectively, whereas and the (-110) crystal facets of CuO had d-spacing value of CuO was 2.45 Å (Fig. 2g). The heterojunction of CuO@TiO_2 is further confirmed by these findings²⁶. The selected area electron diffraction (SAED) pattern in Fig. 2h presented the consistency with the monoclinic CuO $\{-1-1\}$, and $\{111\}$ and P25 TiO_2 for anatase $\{101\}$, $\{200\}$, and $\{204\}$ planes and rutile $\{110\}$ and revealed its polycrystallinity demonstrating that both the planes are present as CuO@TiO_2 heterojunctions (Fig. 2h).

The elemental analysis in the binary system of CuO@TiO_2 nanocomposite were studied by energy-dispersive X-ray spectroscopy (EDS) mapping Fig. 3a endorses the existence of copper (Cu), titanium (Ti), and oxygen (O) elements with the inset displaying an atomic percentage proportion. The EDS mappings of each element are shown in Fig. 3b–e, and they clearly show that this Cu, Ti, and O species are homogeneously distributed throughout the entire selected area, demonstrating the continuous existence of O in the CuO particle and TiO_2 and further through their interface (Fig. 2e). This clearly illustrates the construction of the heterojunction between CuO and TiO_2 , which assists in the transfer of charges between the bands of two semiconductors, CuO and TiO_2 ²⁷.

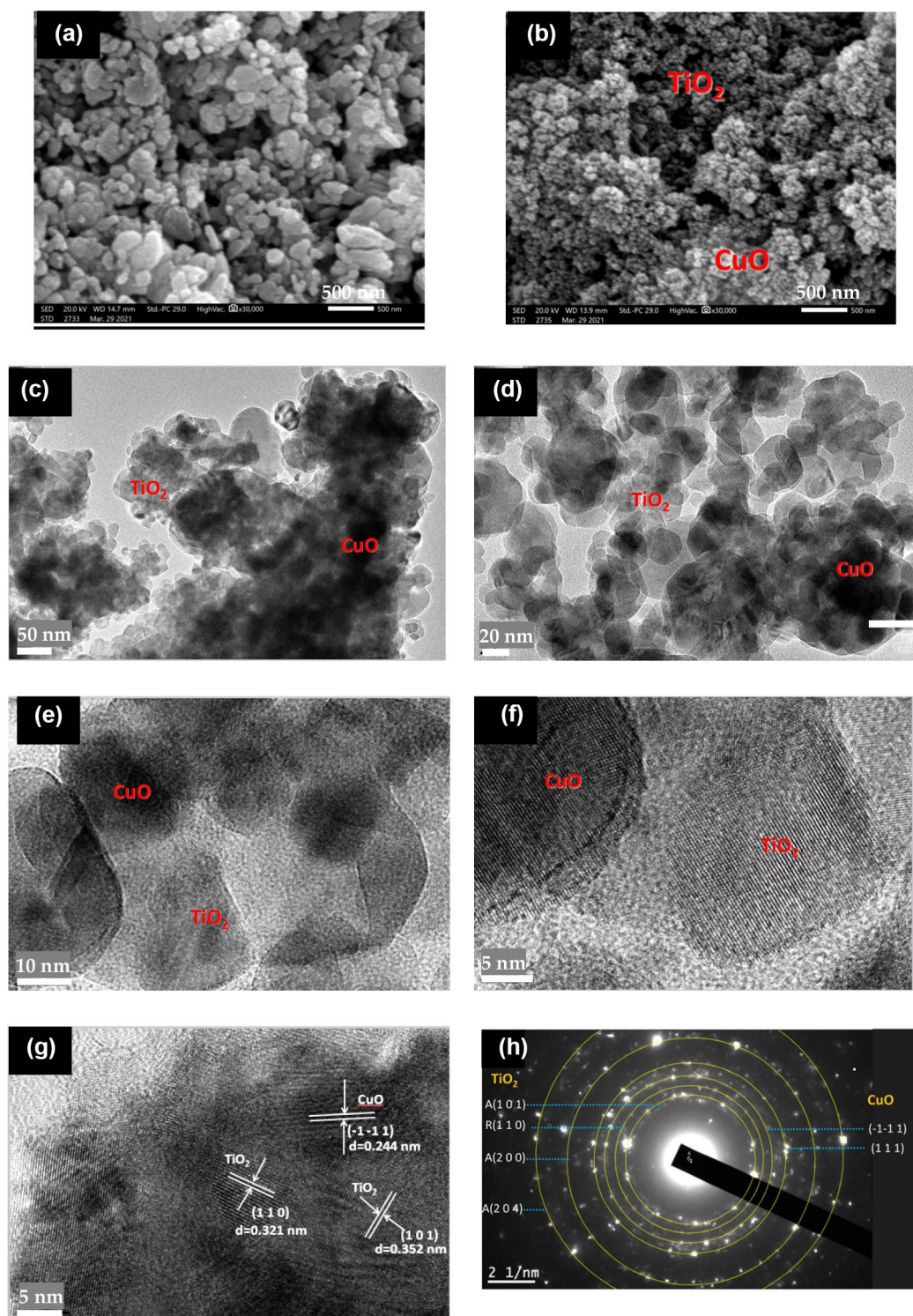


Figure 2. SEM images of (a) CuO, and (b) CuO@TiO₂, (c–g) HR-TEM images of CuO@TiO₂, and (h) SAED of CuO@TiO₂.

Chemical valence states. The chemical surface of pure TiO₂, pure CuO, and its binary system CuO@TiO₂ heterostructure was analyzed by XPS. The high resolution of XPS spectrum of Ti, O, and Cu is displayed in Fig. 4. The binding energy values can be utilized to infer information about Ti chemical and electronic structure states in TiO₂²⁸. As shown in Fig. 4a, the Ti 2p_{3/2} and Ti 2p_{1/2} peaks of Ti⁴⁺ ions in the lattice oxide have binding energies of 458.11 and 463.81 eV, respectively, for CuO@TiO₂. The Ti 2p_{2/3} and Ti 2p_{1/2} binding energies differ by 5.7 eV, indicating that Ti is mainly Ti⁴⁺²⁸. When compared to the binding energies of TiO₂, the small posi-

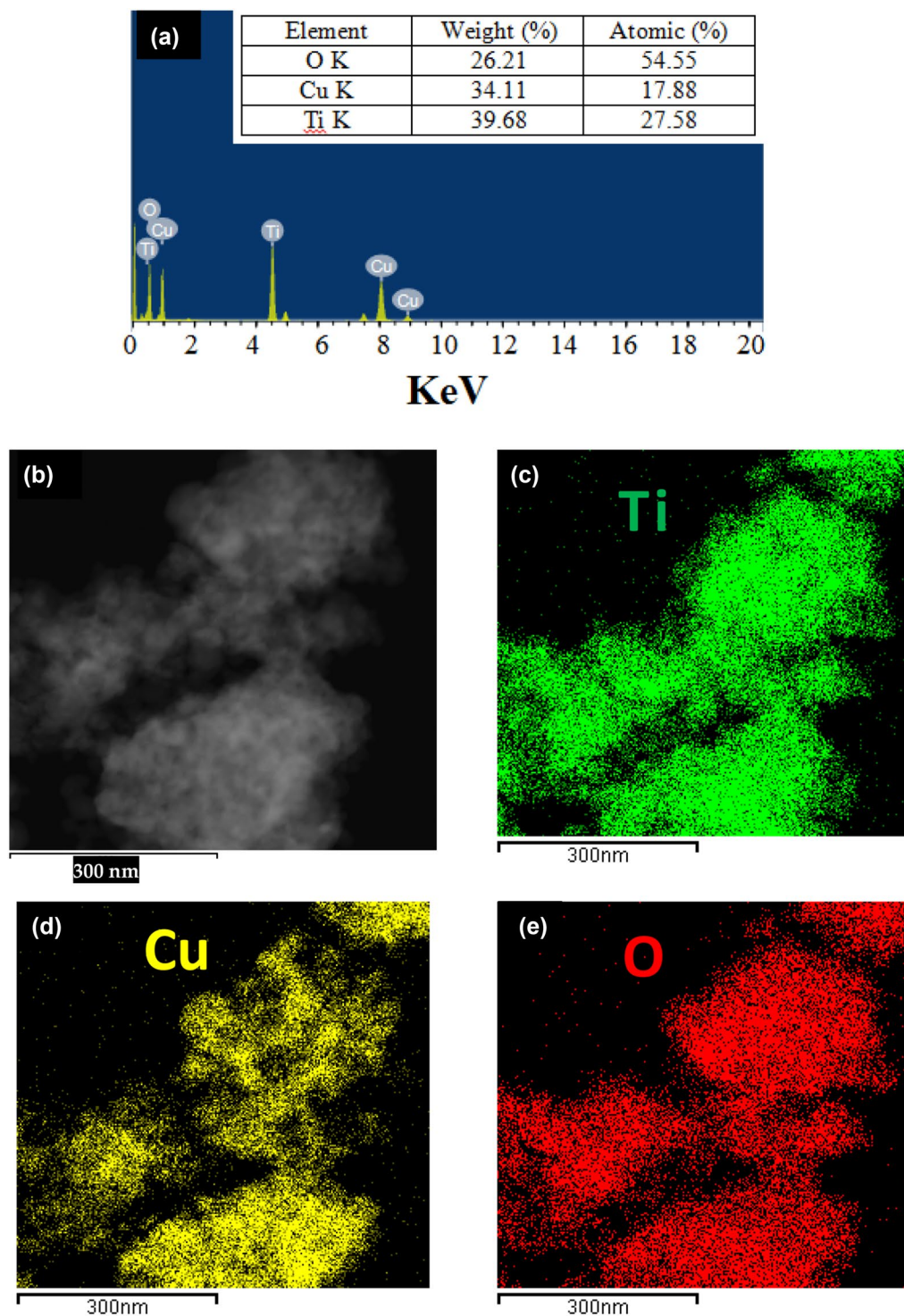


Figure 3. (a) EDS, (b) TEM image, and (c–e) corresponding elemental mapping of binary system of CuO@TiO₂ heterostructure nanocomposites: (c) Ti, (d) Cu, and (e) O.

tive shifts of both Ti 2p_{2/3} and Ti 2p_{1/2} are meaningful of two distinct TiO₂ entities and suggest a variation in the electronic state of Ti in Ti–O^{23,29}. Also, no additional peaks may be observed on the spectra of CuO@TiO₂ in the Ti_{2p} region, which indicates that the addition of CuO is not disturbing the TiO₂ lattice and both oxides exist as separate phases in presented materials³⁰. It also confirms CuO to TiO₂ electron transport at CuO@TiO₂ heterojunction³¹. These results are supported by HRTEM. The only observed change in the Ti 2p XPS image is the decrease of intensity of the peaks, which is the natural consequence of the decreasing concentration of the TiO₂ in the materials with the addition of CuO.

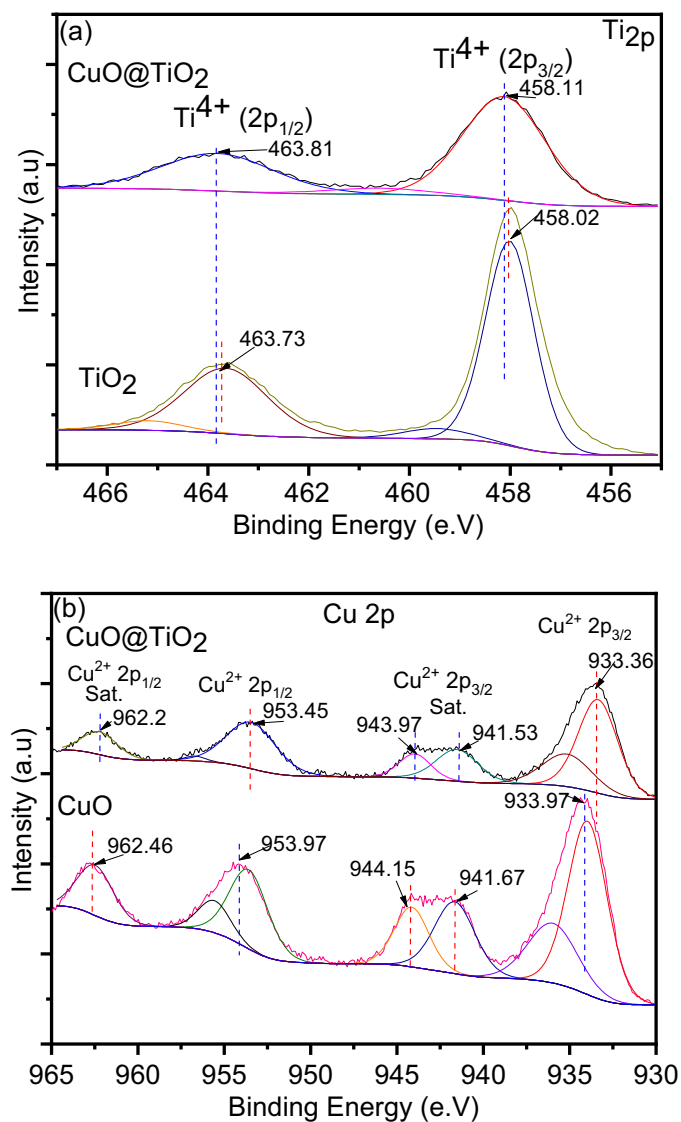


Figure 4. (a) High-resolution XPS scan of (a) Ti 2p, and (b) Cu 2p.

Sample	O _L (%)	O _H (%)	O _V (%)
TiO ₂	71.07 (529.44)	15.56 (530.81)	13.37 (528.86)
CuO	51.1 (529.46)	26.10 (531.01)	22.89 (532.34)
CuO@TiO ₂	24.36 (529.39)	39.77 (530.53)	35.87 (530.94)

Table 1. Species percentage and corresponding binding energies (in brackets, eV) were obtained for TiO₂, CuO, and its binary system CuO@TiO₂.

Based on these assignments, the O_{1s} region on the spectra of TiO₂, CuO, and its binary system shows three peaks after deconvolutions, which resolved to three types of oxygen atoms, the lattice oxygen (O_L), surface hydroxyl groups (O_H), and surface oxygen vacancies (O_V) (Supplementary Fig. S1). The position of O_L is 529.44 and 529.46 eV for TiO₂ and CuO, respectively. The property of O_L was ascribed to the lattice O²⁻ anions bonding to the metal cations in the Ti–O or Cu–O, has the lowest binding energy of O_{1s} at 529.39 eV for CuO@TiO₂³². The broad shoulder at 530.53 eV was linked to the surface hydroxyl groups (O_H) on the surface²⁷, while at peak at 530.94 eV refers to the surface oxygen vacancies (O_V)³³. According to the calculation of peak areas, the concentration of O_V is 35.87% over CuO@TiO₂ is higher than CuO (22.89%) and TiO₂ (13.32%), which is crucial for photocatalytic activity. The chemical composition of various types of oxygen and their percentages are summarized in Table 1.

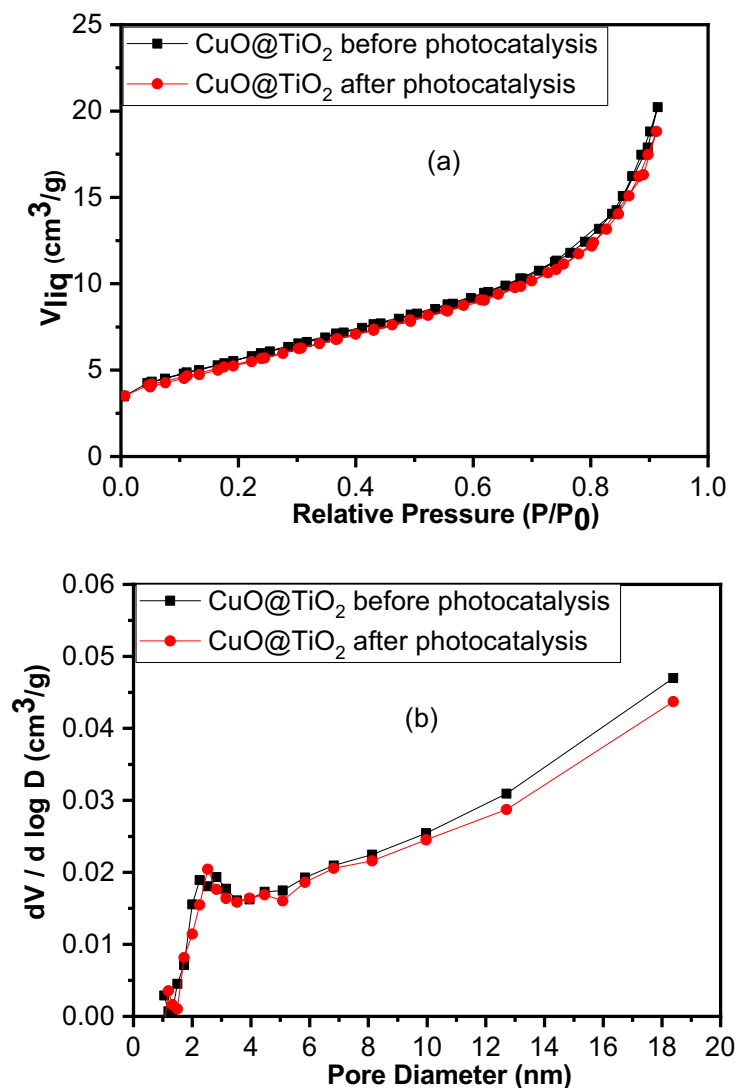


Figure 5. (a) N₂ adsorption/desorption isotherms, and (b) pore diameter distributions of CuO@TiO₂ heterostructure before and after photocatalysis.

From Fig. 4b, there is two prominent peaks at 933.36 and 953.45 eV can be endorsed to Cu 2p_{3/2} and Cu 2p_{1/2}, compared to 933.97 and 953.97 eV for CuO, respectively²³. Also, two addition peaks at 942.66 and 962.2 eV can be assigned to the satellite peaks for Cu²⁺, compared to 941.67 and 962.46 for CuO, respectively. No Cu 2p peaks shift and no additional peaks are forming when TiO₂ concentration is increasing in the CuO. The formation of Cu²⁺ species rather than Cu⁺ in the composite is confirmed by B.E gaps of 20.09 eV¹⁶. The higher binding energy comes from the upshift of Cu_{2p} peak that shows the substantial interaction between CuO nanoparticles and TiO₂ nanoparticles, which is consistent with the literature^{34,35}. Furthermore, there is no peak that relates to Cu⁺ at around 932.7 eV, signifying that Cu species mainly exist as CuO. The existence of an unfilled Cu 3d shell corresponds to the Cu²⁺ species at the CuO surface, as seen by the shakeup satellite peaks with binding energy at 942.66 and 962.2 eV³⁶. This is another proof to endorse the dominant surface copper is CuO in CuO@TiO₂ heterostructure.

In summary, the surface of CuO@TiO₂ photocatalyst is oxidized and functional groups such as OH are incorporated during the calcination. The oxygen vacancies in CuO@TiO₂ form free electrons that lead to creating a reduced form of Ti species (e.g. Ti⁴⁺). This is endorsed by the blue shift of the B_{1g} vibrational mode of TiO₂ (as identified by Raman) and the negative shift of Ti 2p to lower binding energy (as identified by XPS). Based on the XRD, HR-TEM, XPS, and Raman spectroscopy observations, we endorse the existence of TiO₂ and CuO and the successful fabrication of CuO@TiO₂ heterostructure photocatalysts with strong interface interaction.

Textural properties. The textural nature of the catalyst CuO@TiO₂ investigated using BET analysis. The results showed that it has a surface area of 19 m²/g, a total pore volume of 3.12 × 10⁻² cm³/g, and a pore diameter of 6.08 nm. Based on the IUPAC classification, the nitrogen sorption isotherms for the catalyst display the type IV in the shape with H3 hysteresis loop and large adsorption of N₂ at P/P₀ > 0.8 (Fig. 5a). H3 loop indicates the

existence of large mesopores (2–50 nm) with few of micropores³⁷. Figure 5b depicts the plot of the BJH pore-size distribution of the catalyst CuO@TiO₂, which shows that it is essentially mesoporous particles³⁸. The low surface area of CuO@TiO₂ confirms the well-formed crystalline structure, which is extremely important for photocatalytic applications. The high pore volume of the CuO@TiO₂ increases the internal mass transfer and therefore improves the catalytic activity and enhances the photodegradation of AR8.

Optical properties. The band gap of TiO₂, CuO, and its binary CuO@TiO₂ heterostructure catalysts by using the tauc plot are shown in Fig. 6a. It represents the direct transition of band gap energy by plotting $(\alpha h\nu)^2$ versus $h\nu$. As seen, the band gap for P-25 TiO₂ was correspondingly to 3.43 eV, which is caused by the intrinsic interband absorption of TiO₂³⁹. After sintering at high temperature, the Cu₂O color was changed to black, matching the color of the CuO semiconductor. After addition of CuO nanoparticles distinctively displays the lower optical band gap energy of 2.35 eV compared to CuO and TiO₂ of about 2.5 and 3.43 eV respectively. The smaller bandgap of CuO@TiO₂ heterostructure as compared to TiO₂ can be elucidated on the basis of (a) the quantum confinement phenomena, and (b) the existence of CuO favors the formation of oxygen vacancies and/or the partial reduction of Ti sites (as identified by XPS). Taking into account the reduction of Ti sites and/or oxygen vacancies acts as a new state localized in the decreasing of the bandgap. The incorporation of CuO in TiO₂ matrix results in the formation of two closely spaced conduction bands formed by the sharing of interfacial electrons and holes between Cu²⁺ and Ti⁴⁺. Therefore, the enhanced light absorption and interfacial charge transfer will be advantageous for improving the photocatalytic performance of the hybrid photocatalysts^{21,40}. As a result, the latter optical adsorption is extra proof for the presence of CuO classes in the CuO@TiO₂ heterostructure.

To determine the role of photogenerated electron–hole pairs in TiO₂, CuO, and its binary CuO@TiO₂ heterostructure, as well as to demonstrate the mechanism liable for the remarkable boosted photocatalytic degradation of pollutants. Photoluminescence (PL) studies were investigated. The fluorescence emission spectra of samples exhibited a broadband peak at 423 nm under the excitation of 350 nm (Fig. 6b). As we know, the fluorescence intensity of the catalysts tended to be inversely proportional to the rate of recombination rate of e⁻/h⁺⁴¹. As a result, the fluorescence intensity of the pure TiO₂ and CuO is high, indicating a higher photogenerated electron–hole binding rate⁴¹. The modification of TiO₂ by CuO was found to lower fluorescence intensity and more efficient separation of electron and hole by CuO@TiO₂ heterojunction that formed at the interface and therefore accounts for boosting the photocatalytic activity⁴². It also accelerates the creation of e⁻, and extends the lifetime of e⁻/h⁺ lifetime, which was ascribed to the potential well made by the Cu²⁺ hetero-junction to trap electrons⁴³. The separation of electrons and holes results from the electron transfer from TiO₂ to CuO nanoparticles at the interface of CuO (p-type) and the electron-rich of TiO₂ (n-type), which is one possible clarification for the suppressed charge recombination^{44,45}.

Electrochemical properties, EIS. To acquire profoundly thoughtful into the influence of CuO nanoparticles on behaviors of charge transport and reaction rate of the surface of binary system of CuO@TiO₂ composite, the estimation of electrochemical impedance spectroscopy (EIS) was achieved. It is well acknowledged that the smaller arc radius of the first semi circuit matches to a reduced electron-transfer resistance (the low-frequency semicircle), implying the high efficiency of separation and charge transfer⁴⁶, however second semi circuit is attributed to recombination resistance (the high-frequency semicircle) in p–n junction of photovoltaic devices in the fitting EIS spectra (Fig. 6c). The semicircular in EIS plots for all samples indicate the same behavior. Furthermore, the equivalent electrical circuit was shown as inset and the collected values of ohmic series resistance (R_s), charge transfer resistance (R_{ct}), recombination resistance (R_{rec}), and interface resistance were detailed in Table 2. Among all results the CuO@TiO₂ show a significantly smaller charge transfer resistance R_{ct} (1372 Ω) than both of TiO₂ (1476 Ω) or CuO (3074 Ω), which suggests that CuO@TiO₂ has the fastest electron–transfer rate^{47,48}. Comparing with bare CuO and bare TiO₂, the binary system of CuO@TiO₂ suggests the higher separation efficiency of photoinduced e⁻/h⁺ pairs at the interface, faster interfacial charge transfer, and more efficient separation of electron–hole pairs^{46,49}. On the other hand, the CuO@TiO₂ shows higher recombination resistance than TiO₂ which confirms that the additional CuO interface of the binary system of CuO@TiO₂ prevents the excited electrons from recombination in TiO₂. It is worth to mention, that the equivalent electrical circuit present also very high interface resistance for both TiO₂ (315 Ω) and CuO (1383 Ω) compared to the binary system CuO@TiO₂ (4 Ω). Therefore, the lower charge transfers resistance and higher recombination resistance of CuO@TiO₂ favored a higher photocatalytic activity.

Computational calculations. The DFT calculations are commonly regarded as crucial to comprehending the behavior of chemical structures. We presented four possible configurations based on the XRD results (TiO₂, Cu@TiO₂, Ti@CuO, and CuO) that might exist as illustrated in Fig. 7. The computational calculations were performed to relax all possible structures and estimate the charge distribution and electronic properties as well^{50–52}. Along best-fit plane's charge density distributions for the four possible configurations were carried out. The resulting data display a small displacement of Ti/Cu positions along with the surface interaction of both materials and combined with an increase in a bond length of Ti–O and Cu–O for both Cu@TiO₂, Ti@CuO, respectively.

The experimental energy gap results of diffuse reflectance spectra are inconsistent with the preformed band structure calculations (Fig. 8). The band diagram shows an indirect bandgap for TiO₂ and proposed Cu@TiO₂ (surface interaction) from X to G symmetry point, along with the crystal symmetry directions in the first Brillouin zone. Similarly, the findings reveal a direct bandgap for both CuO and Ti@CuO at the G symmetry point. Meanwhile, the computed bandgap values show a gradual decrease with increasing Cu and Ti substitution ratio in both surface interaction configurations of Cu@TiO₂ and Ti@CuO, respectively. Thus, the findings

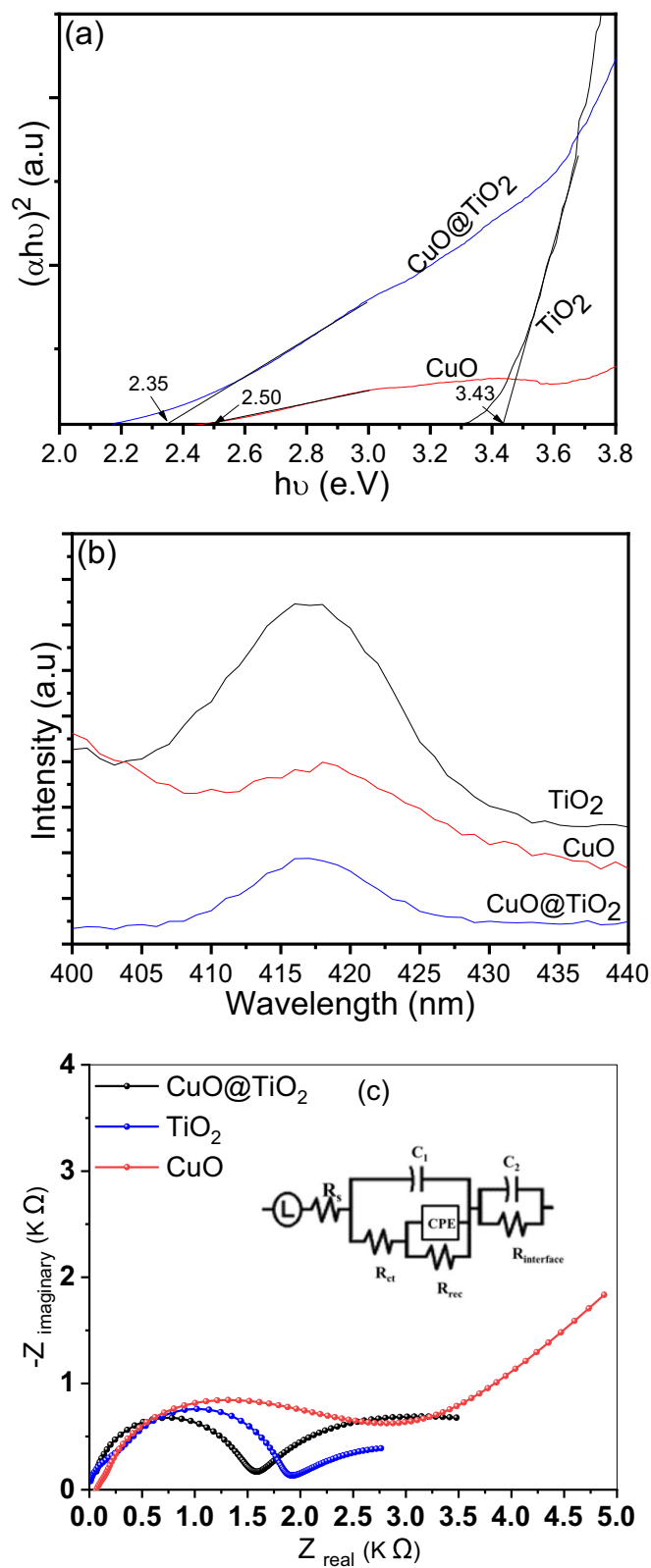


Figure 6. (a) Tauc plots of the band gap, (b) Photoluminescence spectra, and (c) EIS profile of photocatalysts.

Photocatalyst	R_s (ohm)	R_{ct} (ohm)	R_{rec} (ohm)	$R_{interface}$ (ohm)	X^2
TiO ₂	0.1	1476	1992	315	0.01
CuO	21	3074	1.6E15	1382	0.01
CuO@TiO ₂	46	1372	3391	4	0.001

Table 2. Ohmic resistance values obtained from the EIS analysis of TiO₂, CuO, and its binary system of CuO@TiO₂ heterojunction. (Where: R_s (series resistance), R_{ct} (charge transfer resistance), R_{rec} (recombination resistance)).

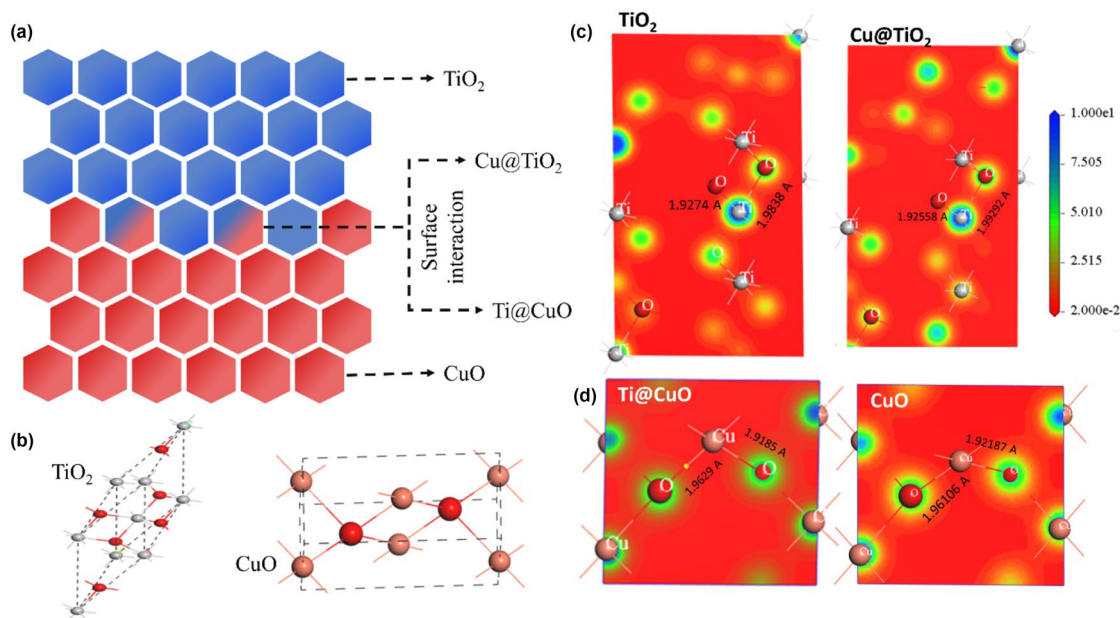


Figure 7. (a) Simulated surface interaction of (a) CuO and TiO₂; Crystal structure unit cell of (b) both TiO₂ and CuO; charge density distribution at the best fit plan for both (c) TiO₂, (d) CuO and two proposed surface interaction Cu@TiO₂ and Ti@CuO as well (Cu–O and Ti–O bond length by angstrom Å).

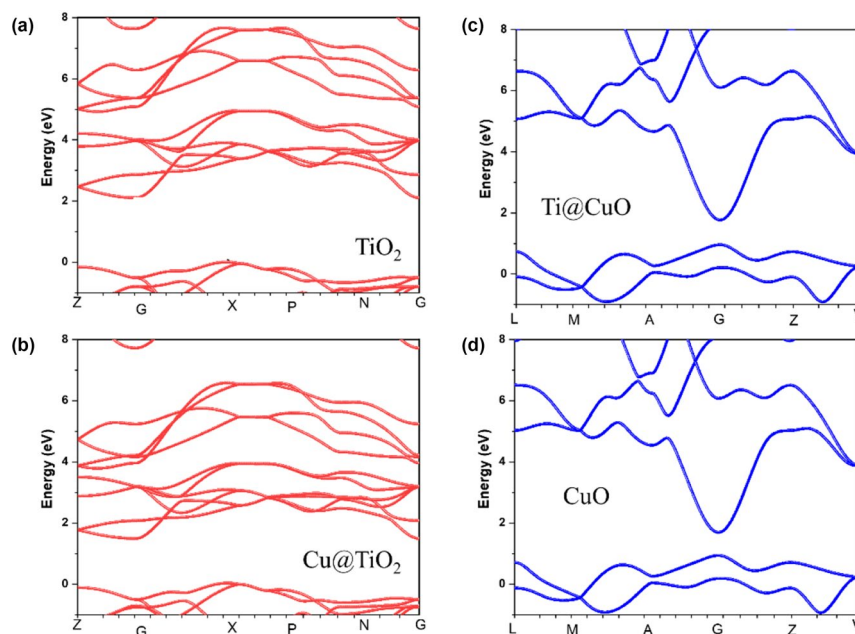


Figure 8. Bandstructure diagram of four proposed configurations (a) TiO₂; (b) Cu@TiO₂; (c) Ti@CuO; and (d) CuO.

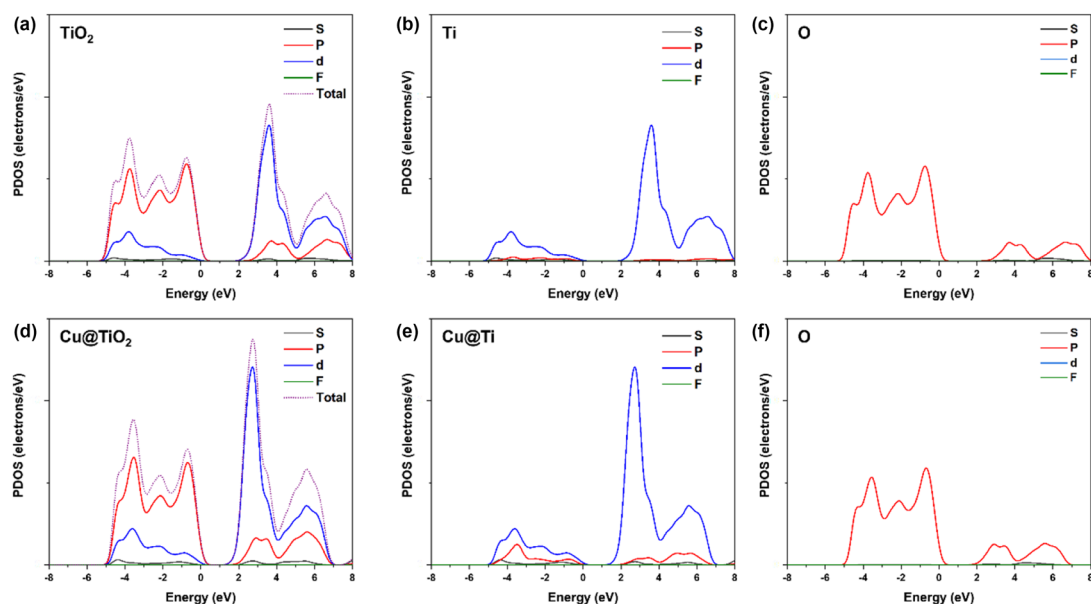


Figure 9. TDOS of (a) TiO_2 ; PDOS of TiO_2 based on (b) Ti and (c) O^- (d) TDOS of Cu@TiO_2 ; PDOS of Cu@TiO_2 based on (e) Cu/Ti $^-$ and (f) O.

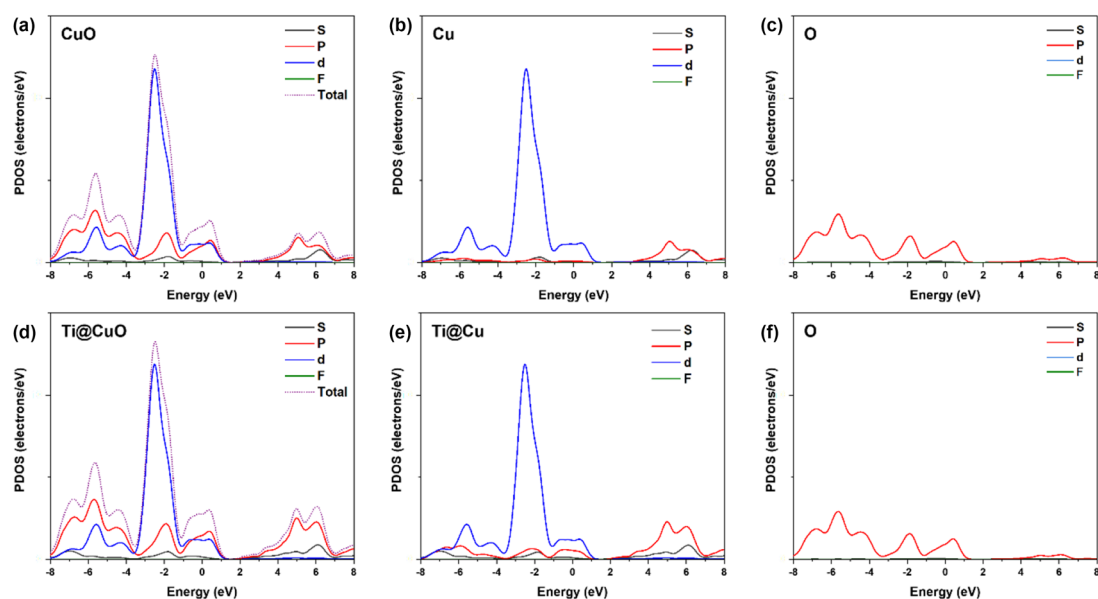


Figure 10. TDOS of (a) CuO ; PDOS of CuO based on (b) Cu and (c) O. TDOS of (d) Ti@CuO , PDOS of Ti@CuO based on (e) Ti/Cu and (f) O.

confirm the UV-Vis results and also predict enhancing of the performance of prepared catalysts toward photodegradation applications.

However, the TDOS result (Fig. 9) for the configurations of TiO_2 , and Cu@TiO_2 show a major contribution of antibonding d -orbital at the minimum CB and p -orbital at the maximum VB. For more clarifications, the partial density of state (PDOS) of Ti and O atoms of TiO_2 indicates that the main contribution at maximum VB depends on the p orbital of O atoms, Meanwhile the d -orbital of Ti at the minimum CB. Similarly, Cu doped Cu@TiO_2 refers to the contribution of the same orbital with a significant effect at minimum CB toward lower bandgap which clarifies the reason behind that.

The total density of state (TDOS) for CuO and Ti@CuO (Fig. 10) refer to a probability of (p and d) orbitals contributes in the VB and d -orbital at the minimum of the CB. However, PDOS of Oxygen (O), and Copper (Cu) atoms of CuO show that at maximal VB, the main contribution is dependent on both p -orbital of O, and d -orbital of Cu atoms. Also, the p -orbital of Cu has a main contribution at the minimum conduction band without any sign of contribution of O atoms in conduction band. Likewise, Ti doped Ti@CuO at the surface interaction refer

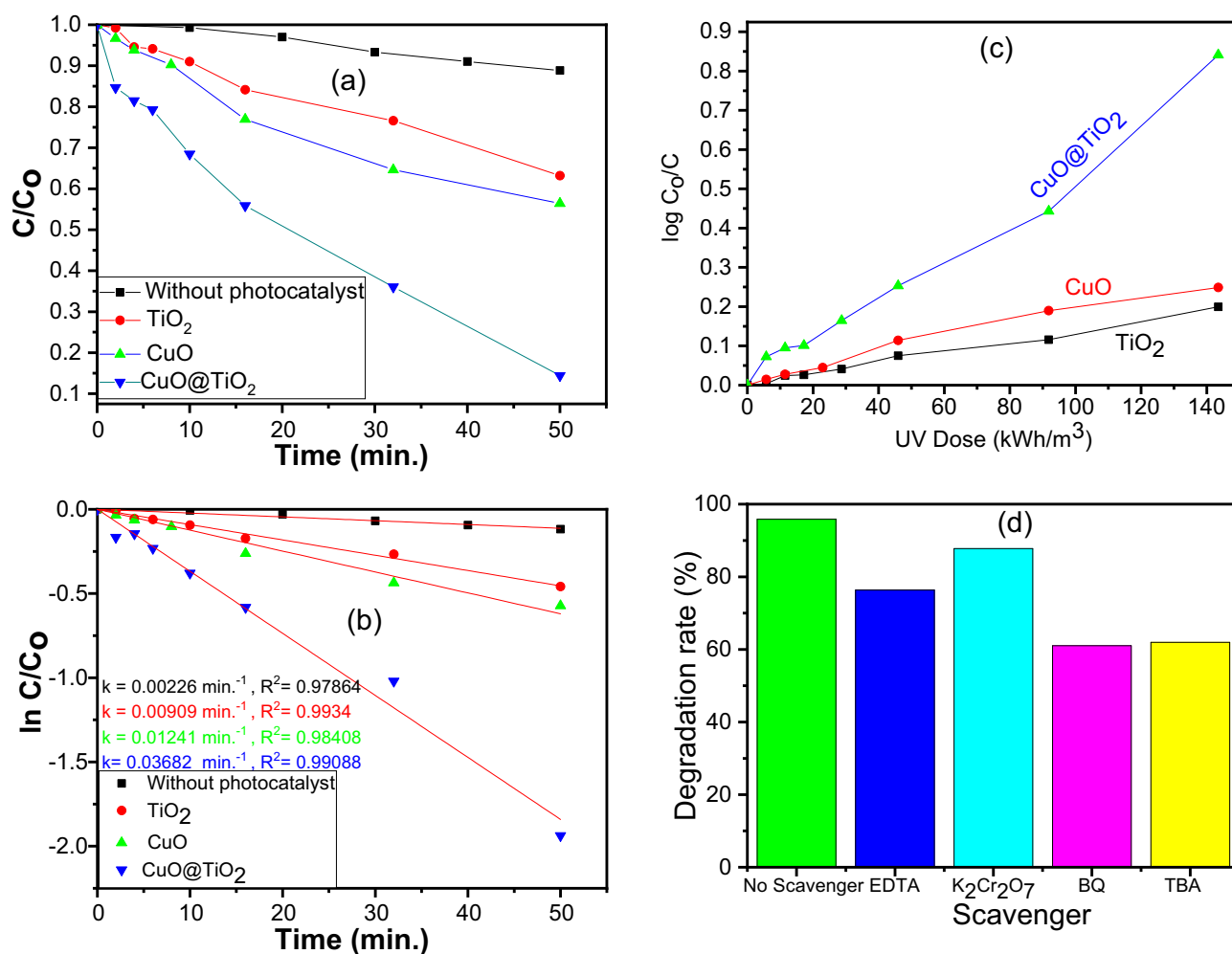


Figure 11. (a) The change in the concentration of Acid Red 8 dye as a function of exposure time (b) kinetic model of the Acid Red 8 photocatalytic degradation, (c) Change of $\log(C_0/C)$ with UV dose for degradation of AR8 dye with different photocatalysts, and (d) Photocatalytic activity of AR8 dye over the CuO@TiO₂ in the presence of different scavengers.

to the same orbitals with a significant contribution at maximum VB. Thus, these results at the surface interaction of CuO–TiO₂ configuration predict that a significant enhancement of CB to decrease the band gap. However, because of the contribution of copper atoms to enhancement of maximum VB in the existence of the *p*-orbital of titanium atoms, could achieve the charge transfer due to S-scheme mechanism and resulting in an increase in the attract of excited electrons of CuO and the holes of TiO₂ as well, during photocatalytic degradation process.

Photocatalytic activity. Kinetic studies. The photocatalytic degradation of Acid Red 8 (AR8) aqueous solution was assessed using batch mode. Figure 11a shows the catalytic activities of without catalyst (UV only), TiO₂, CuO, and its binary CuO@TiO₂ heterojunction composites. The photocatalytic activity of the CuO@TiO₂ was found to be substantially higher than those of TiO₂ and CuO nanoparticles. The photocatalytic degradation of AR8 has also followed the pseudo-first-order kinetic model (Fig. 11b). Kinetic curves also highlight CuO@TiO₂ exhibits 3.08 and 4.11 times the photodegradation ability of CuO and TiO₂, respectively (Table 3). Also, the $t_{1/2}$ decreases with increasing the apparent rate constant (k_{app}) as shown in Table 3.

The low decomposition rates of CuO and TiO₂ nanoparticles could be attributed to the fast recombination of e^-/h^+ pairs and inefficient quantum yield during the photocatalytic processes. The superiority of CuO@TiO₂ binary system is due to the efficient charge transfer, enlarged light response range, and suppressed the photo-carrier recombination that originated from the synergistic effects of two photocatalysts, TiO₂ and CuO that resulted from p-n heterojunction between p-type CuO and n-type TiO₂⁵³. Photogenerated holes diffuse from CuO (p-type) to TiO₂ (n-type) and electrons diffuse from TiO₂ to CuO due to the existence of carrier concentration gradients. An electric field is formed at the junction when it is in the equilibrium⁵⁴.

Photogenerated electrons can migrate the conduction band of TiO₂ (n-type) and holes to the valence band of CuO (p-type) during photocatalysis. The p-n CuO@TiO₂ heterojunction increases the photocatalytic activity by facilitating the separation of photogenerated electrons and holes. Additionally, the sensitization by CuO increased the optical absorption properties of TiO₂ and improved charge carrier lifetime in the system that leads to enhancing the photocatalytic activity of CuO@TiO₂. As indicated by XRD, HR-TEM, XPS, UV-Vis., PL, and

Photocatalyst	k_{app} (min ⁻¹)	$t_{1/2}$ (min.)	E_{EO} (kWh/m ³)	Q_{app} (%) (mol/Einstein)
TiO ₂	0.00909	77	769.2	0.782
CuO	0.01241	57.75	526.3	1.035
CuO@TiO ₂	0.03688	18.73	172.4	3.20

Table 3. Collective data of apparent rate constants, half lifetime, electrical energy per order, and apparent quantum yield for degradation of acid red 8 dye using TiO₂, CuO, and its binary system of CuO@TiO₂ heterojunction.

EIS characterizations as well as DFT investigations, heterojunction formation considerably influenced the photocatalytic activity of CuO@TiO₂ due to its influences on the photocatalyst microstructure and band structure.

Quantum efficiency. The quantum yield can be detected by estimating the rate of disappearing of the reactant molecule or the formation of the product molecule divided by the photons absorbed per unit time, which can be used to quantify the heterogeneous catalysis. A considerable portion of the incident light is reflected or scattered by dispersed photocatalysts and is not absorbed by the dye solution. In most cases, there is no way to measure the amount of light absorbed by the photocatalyst experimentally. Another parameter frequently stated is the apparent quantum yield (Q_{app}), which avoids the challenges of estimating the quantum yields in the photocatalytic reaction⁵⁵.

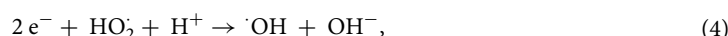
Table 3 clarifies that Q_{app} for UV/CuO@TiO₂ system is higher than that of the UV/TiO₂ and UV/CuO systems. As a result of the poor quantum yield, CuO and TiO₂ nanoparticles had the lowest photocatalytic activity.

Investigations of E_{EO} . The economic analysis of photocatalysis is critical factor that accounts for a large portion of operating costs. As a result, it is vital to evaluate the photocatalytic process' electrical energy consumption under experimental settings. Because it follows the pseudo first order kinetic model, the electrical energy per order (E_{EO}) is a useful indicator of the photocatalysis process⁵⁶. The E_{EO} enables a quick calculation of the cost of electrical energy and indicates the overall power needed. The treatment efficiency for the samples is evaluated using E_{EO} values for comparative study.

The E_{EO} values were calculated using the inverse of the slope of a plot of $\log(C_0/C)$ versus UV dose (Fig. 11c). It was determined that the figure-of-merit method is appropriate for calculating the electrical energy efficiency. It is not only demonstrating the decline in the amount of electricity required by the photocatalytic system, but also the significant impact of the UV dose on the E_{EO} in the process. From Table 3, the E_{EO} values were established to be depending on the photocatalyst's nature. Furthermore, the E_{EO} values of the UV/CuO@TiO₂ system are lower than those of the blank UV/TiO₂ or UV/CuO system, indicating that the lower energy consumption is attributable to the higher applied potential and formation of highly reactive radical species. In summary, these insights can be used to design photocatalytic systems that use less electrical energy, have a higher rate constant, and cost less to operate.

Role of reactive oxygen species. To get insights into the photodegradation mechanism of AR8 dye over the CuO@TiO₂ binary system and understand the role of photo-generated holes and radicals in the photodegradation process, the charge trapping studies were conducted. To explore the role of reactive oxygen species (ROS), the photocatalytic activity of CuO@TiO₂ was greatly suppressed by the addition of EDTA, K₂Cr₂O₇, benzoquinone (BQ), and tert-Butyl alcohol (TBA) as model scavengers to capture holes (h^+), electron (e^-), superoxide radical (O_2^-), and hydroxyl radical ($\cdot OH$), respectively⁵⁷. The AR8 degradation efficiency by CuO@TiO₂ in the existence of various scavengers is shown in Fig. 11d. Both BQ and TBA had stronger suppressing effects on the photocatalytic degradation of AR8 than that for EDTA and K₂Cr₂O₇, suggesting that O_2^- and $\cdot OH$ are the principal active species in the photocatalytic degradation of AR8 in the presence of a binary system of CuO@TiO₂.

Based on the outcomes of the trapping tests, the following Eqs. (1–6) can be offered as a possible photodegradation mechanism of AR8 dye in the presence of CuO@TiO₂ heterojunction.



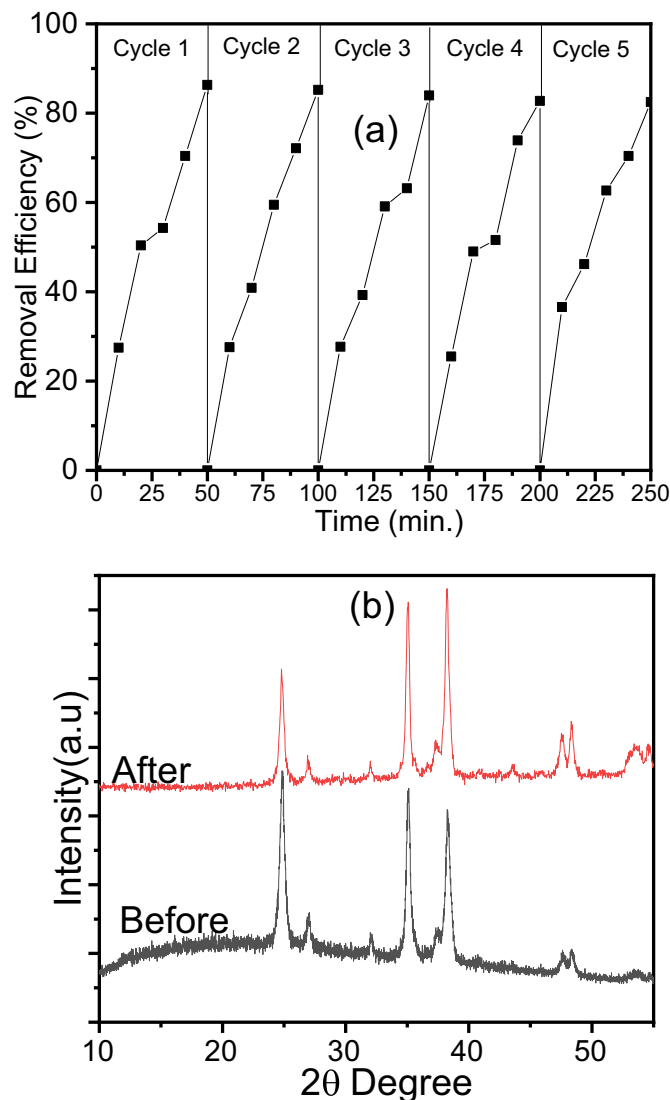


Figure 12. (a) Cycling runs, and (b) XRD before and after photocatalytic degradation of AR8 dye over CuO@TiO₂.

Stability and recyclability of CuO@TiO₂ photocatalyst. From the economic point of view, the stability and good recyclability are two essential features for large-scale application of photocatalysis⁵⁸. Using the same protocol, the degradation of AR8 were done on subsequent repeated cycles by reusing the CuO@TiO₂ collected after each cycle. Then, the degradation percentage was calculated in each run. The stability and recyclability of CuO@TiO₂ towards AR8 dye photodegradation were evaluated after five consecutive runs and the obtained data are presented in Fig. 12a. It is clear that the reduction in the removal efficiency was negligible (<4.5%), which denotes the nature of high stability after 5 cycles. Wherefore, CuO@TiO₂ is an economically suitable photocatalyst for industrial application from a practical point of view.

To evaluate the stability of CuO@TiO₂ photocatalyst, the XRD patterns were compared before and after the first cycle of the photocatalytic degradation of AR8 dye as shown in Fig. 12b. Obviously, the maintained structure after photocatalysis was evidenced by the unchanged XRD reflections. All peaks corresponding to the interpretation based on Fig. 1a, represent the stability of CuO@TiO₂.

As it is known, the porous structure is one of the most important requirements for the ideal photocatalysis process. Table 4 shows the textural nature of sample CuO@TiO₂ and its recycled sample after photocatalysis that was investigated by BET analysis (Fig. 5). There is a slight decrease in the surface area after recycling indicating low structural changes occurrence by recycling (Table 4). The pore volume and pore diameter were also slightly reduced. Even after the recycling, the catalyst still had a feasible pore diameter that can accommodate the flow of reactant intermediate molecules) through the photocatalyst during the reaction. S_{BET} surface area based on BET equation, S_{micro} micropores surface area, L_0 micropore width, V_T total pore volume, V_{meso} mesopores volume.

To discuss the mechanism of the photocatalytic reaction for CuO@TiO₂, an XPS analysis was investigated the elemental valence states on the surface of CuO@TiO₂ before and after AR8 removal. The changes of element

Samples	S_{BET} ($\text{m}^2 \text{g}^{-1}$)	S_{micro} ($\text{m}^2 \text{g}^{-1}$)	L_o (nm)	V_T ($\text{cm}^3 \text{g}^{-1}$)	Pore diameter (nm)	V_{meso} ($\text{cm}^3 \text{g}^{-1}$)
Before	19	34	3.52	0.0312	6.08	0.007
After	18	32	3.48	0.0291	6.01	0.006

Table 4. Textural characteristics of the CuO@TiO₂ before and after photocatalysis.

state before and after the photocatalytic reaction are revealed in Fig. 13 and Table 5. Figure 13a shows that the O_{1s} peaks of CuO@TiO₂ were divided into three peaks. After photocatalysis, the peak at 529.39 eV belonged to the lattice oxygen (O_L), including Ti–O and Cu–O, was shifted to 529.07 eV²⁹. Also, the peak at 530.94 eV attributed to ions O₂[−] staying in the oxygen vacancy (OV) that is shifted to 530.84 eV. The peak at 530.53 eV was attributed to hydroxyl oxygen (O_H) that shifted to 530.76 eV after photocatalysis. The relative ratios of elements for catalysts have been calculated and are shown in Table 5. The oxygen content in TiO₂ and CuO mainly composed of O_L, and the proportion of O_H and O_V is very small (Table 1), which reduced to 24.36% in the composite. After photocatalysis, the concentration of O_L is reduced to 10.02%, which confirmed the contribution of O_H and O_V in the photocatalytic process (Table 5) and supported the results of the role of reactive oxygen species (Fig. 11d) and photodegradation mechanism (Eqs. 1–6). Furthermore, CuO@TiO₂ displayed lower O_H than before photocatalysis, which was ascribed to the high oxidation ability of the CuO@TiO₂ structure (Table 5). Also, CuO@TiO₂ displayed much higher oxygen vacancy (O_V/O) than before photocatalysis, which was attributed to the greater loss of lattice oxygen by TiO₂ nanoparticles to introduce more oxygen vacancies to the composite (Table 1).

After UV illumination, Fig. 13b show the peaks of Cu 2p_{3/2} and Cu 2p_{1/2} moved to 932.76 and 952.71 eV, respectively, being assigned to Cu⁺⁵⁹. These revealed that most of surface Cu²⁺ was reduced to Cu⁺ upon the UV irradiation⁶⁰. The photocatalytic process introduced more oxygen vacancies on the surface of CuO@TiO₂, which is reflected in Table 5. Under UV light irradiation, the electron can transfer from the valence band to the surface CuO through interface charge transfer, leading to the reduction of Cu²⁺ to Cu⁺³.

After photocatalysis, the 457.75 and 463.75 eV positions were assigned to typical Ti 2p_{3/2} and Ti 2p_{1/2} peaks in CuO@TiO₂, respectively, which indicate there is a small shift of all peaks when compared to the composite before photocatalysis (Fig. 13c). This shift of binding energy values is attributed to the redistribution of electric charge in the composite materials⁶¹. In addition, the spectra of Ti 2p region showing the presence of Ti³⁺ that formed from the reduction of Ti⁴⁺ and denoting the influence of UV light on the nature of the Ti phase, in agreement with TiO₂ results previously reported²⁸. Despite the certain reduction observed the difference in BE between Ti 2p_{3/2} and Ti 2p_{1/2} components are always maintained at 5.7 eV.

Structure activity correlation and proposed photocatalytic mechanism. The plausible mechanism of the photocatalytic degradation of AR8 dye over CuO@TiO₂ heterojunction composite is proposed in Fig. 14 based on the aforementioned experimental findings and characterization analysis. In this system, upon direct irradiation, the e[−]/h⁺ pairs would be formed on both TiO₂ and CuO. In the transfer process, the lifetime of the excited electrons and holes is extended, resulting in better quantum efficiency (Table 3).

Furthermore, this considerably improves the separation of the photogenerated electron–hole pairs and limits their quick recombination, resulting in CuO@TiO₂ having a higher photocatalytic activity than TiO₂⁵⁶. When the combination of TiO₂ with CuO, an inner electrical field forms at the interface lead to improving the electron–hole separation⁶².

Because of TiO₂ of lower EF and connected with CuO of higher EF, the CuO@TiO₂ heterojunction is formed. However, the electrons will transfer from CuO to the TiO₂ easily until the EF at the interface tends to equilibrate. Concurrently, CuO shows downward interface band bending and is positively charged at the interface owing to loss of electrons; while TiO₂ shows upward interface band bending and is negatively charged at the interface owing to an accumulation of electrons. Meanwhile, the electrons transfer creates an internal electric field at interfaces pointing from CuO to TiO₂. When the CuO@TiO₂ heterojunction is exposed to light, under the combined effect of an internal electric field, interface band bending and Coulomb interaction, the photogenerated electrons in CB of TiO₂ easily transfer to VB of CuO and recombine with the photogenerated holes of CuO. Meanwhile, the photogenerated holes on VB of TiO₂ and the photogenerated electrons on CB of CuO are maintained, which participate in the photocatalytic redox reaction, respectively^{63–66}.

Because CuO's conduction band is more negative than TiO₂'s, photo-generated electrons have an affinity to transfer from CuO's conduction band to TiO₂'s conduction band because of the difference in potential, reducing the possibility of photoinduced e[−]/h⁺ recombination and thus facilitating reduction reactions for the destruction of pollutants⁶⁷. Meanwhile, because TiO₂'s VB is more positive than CuO's, the holes transfer from TiO₂'s VB into CuO's VB, which carry out oxidation reactions with water to form a proton and intermediate products. This causes the photogenerated electrons to be accumulated at the conduction band of TiO₂ and also to be accumulated of holes at the valence band of CuO. As a result of the higher conduction and valence band of CuO than TiO₂, the transfer process is thermodynamically advantageous^{68,69}. Hence, the e[−]/h⁺ pair recombination rate in the CuO@TiO₂ is substantially lower than in pure TiO₂. Furthermore, the electrons help Ti³⁺ ions in having a longer lifetime and improve ions transference at the interface between CuO and TiO₂. Overall, the p–n heterojunction may prevent the recombination of the photogenerated electrons from recombining with holes.

According to the abovementioned results of the effect of reactive oxygen species and the results from XPS before and after photocatalysis, the ongoing electrons reduced dissolved oxygen, generating 'O₂[−] (Eq. 2) and the following 'OH (Eq. 4) which was the governing active species for the pollutant attacking that consistent with the results of effect of scavengers (Fig. 11d). On the other hand, the holes stay in the VB of CuO that helps in the

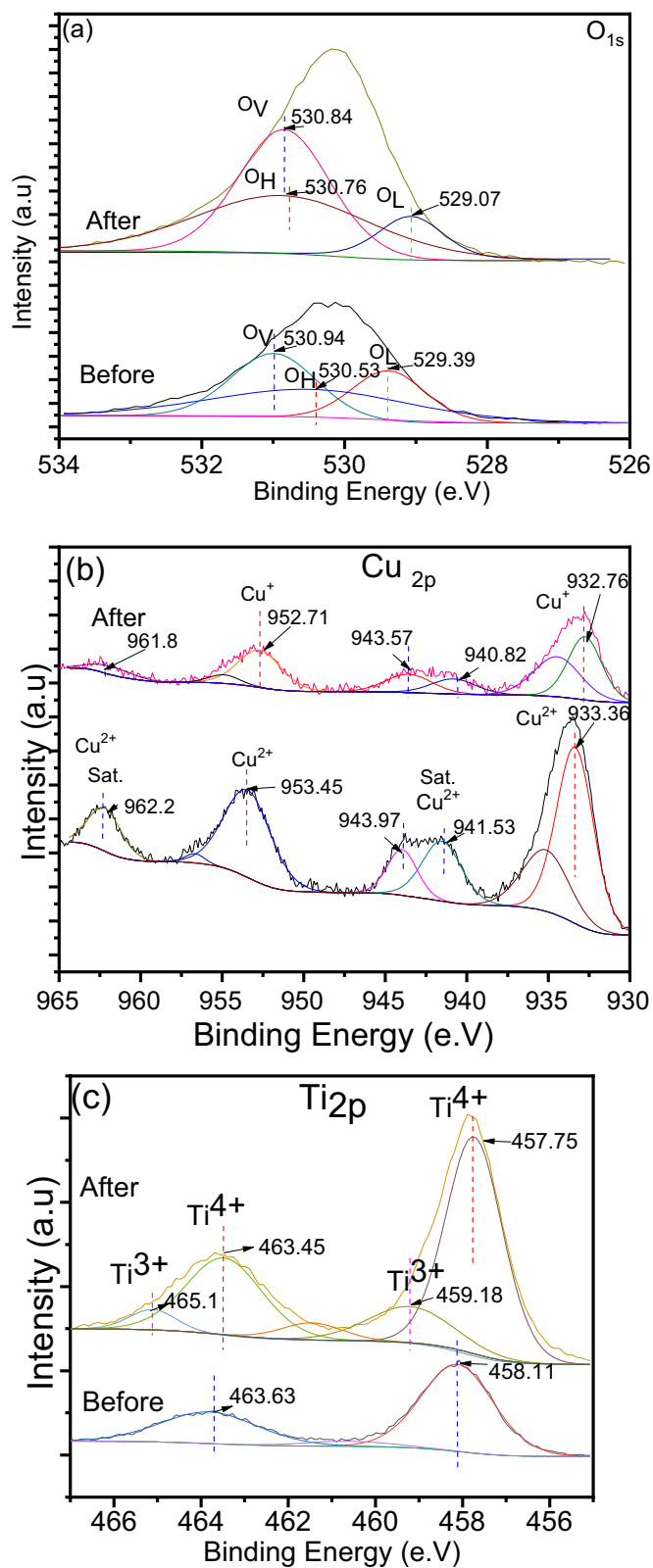


Figure 13. XPS of (a) O1s, (b) Cu2p, and (c) Ti 2p of CuO@TiO₂ before and after photocatalysis.

conversion of OH⁻ to ·OH which leads to the effective degradation of AR8 dye by the direct oxidation of photo-generated holes. The AR8 dye can be destroyed in two ways. (i) in the VB of CuO, the conversion of hydroxyl

Sample	O _i /O	O _H /O	O _v /O
Before	24.36	39.77	35.87
After	10.02	35.26	54.71

Table 5. The relative oxygen content for CuO@TiO₂ before and after photocatalysis.

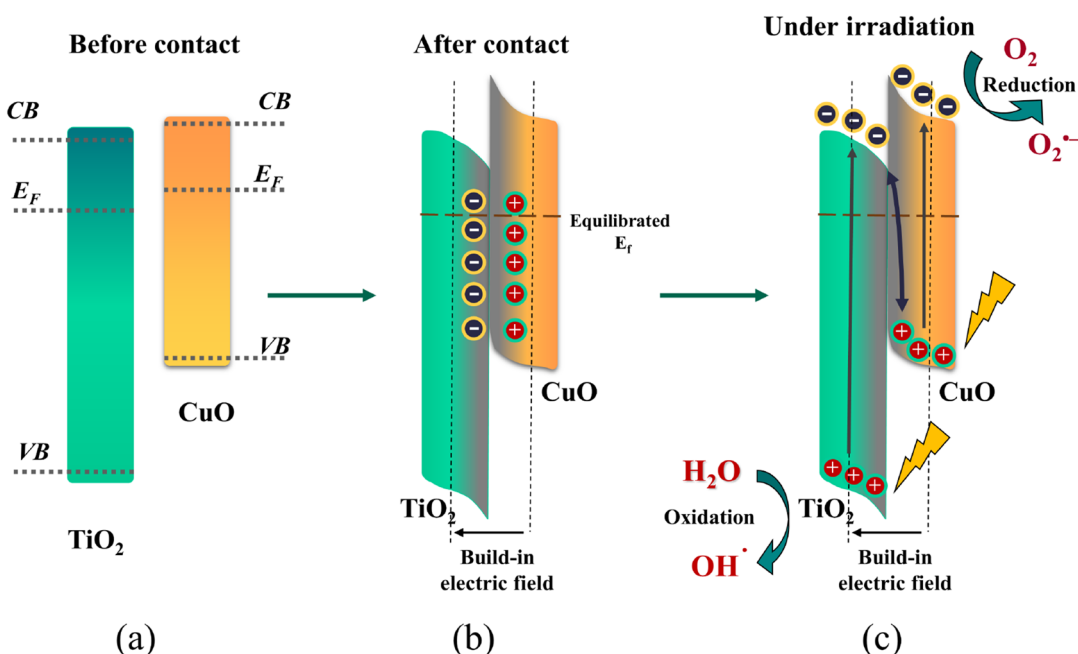


Figure 14. Schematic illustration of the S-scheme transfer mechanism between TiO₂ and CuO (a) Before contact, (b) After contact, and (c) After contact in light. CB conduction band, VB valence band, E_F fermi level.

anion (OH^-) to hydroxyl radical ($\cdot\text{OH}$) (Eq. 5); and (ii) the formed electrons from the CB of TiO₂ are transferred to the adsorbed oxygen ($\text{O}_{2\text{ adsorbed}}$) for generation of superoxide anion radical ($\cdot\text{O}_2^-$) (Eq. 2). Continuous production of highly strong oxidants ($\cdot\text{O}_2^-$ and $\cdot\text{OH}$) leads to the oxidation AR8 to CO₂ and H₂O²¹.

According to the thoughts presented above, the highly boosted photocatalytic activity of CuO@TiO₂ heterostructures compared to pure TiO₂ can be attributed to a number factors, including the intensification in the photo-absorption, perfection in the charge separation efficiency and direct oxidation of AR8 dye with CuO after the construction of p-n heterojunctions. The synergistic impact (for example, heterojunction-induced effects on CuO@TiO₂ photocatalysts) can aid to strengthen the separation of photo-generated electrons and holes (Fig. 14). As a result, the CuO@TiO₂ composites outperform ordinary TiO₂ in terms of photocatalytic activity. Another benefit for photocatalytic decomposition by CuO@TiO₂ heterojunction nanocomposite is to form electrons that help Ti^{3+} ions for extending the lifetime and improve the transfer of electrons at the p-n junction which suppresses the electron/hole recombination.

Materials and chemicals

TiO₂ (Degussa P 25, average particle size about 30 nm, 70% anatase form and of surface area about 50 m² g⁻¹) was purchased from Degussa company, Germany. CuCl₂·2H₂O, NaOH and glucose were purchased from Aldrich. All aqueous solutions were prepared using distilled water from the Millipore instrument. Acid red 8 dye with molecular formula C₁₈H₁₄N₂Na₂O₇S₂, and molecular weight of 480.42 g/mol, with λ_{max} 508 nm was purchased from Fluka.

Synthesis of photocatalysts. CuO nanoparticles were prepared by free-template method by dissolving 1 g of copper precursor in 50 mL solvent (water/ethanol) under a constant stirring at room temperature. A precipitate was produced when NaOH solution (3 M, 10 mL) is added dropwise to the above solution. After being stirred for 5 min, D-glucose powder (0.2 g) was added into the dark precursor and the temperature was raised up to 70 °C with stirring for 15 min. The precipitate gradually turns into brick red and then it was allowed to cool to room temperature and the obtained precipitates were centrifuged. The precipitate was allowed to centrifuge twice more in de-ionized water and anhydrous ethanol, respectively. Finally, the precipitates product was dried at 50 °C overnight.

The S-scheme CuO@TiO₂ heterojunction nanocomposite was prepared through a solid-state reaction route. 50 wt. of Cu₂O nanoparticles were added to 50 wt.% TiO₂ which have been mixed uniformly and made fine by

grinding in ball mill for 2 h to get fine nanopowders. The resultant powders were calcined in air at 500 C for 3 h in an electric muffle furnace.

Correlation between physicochemical characteristics and photocatalytic activity. The detailed of physicochemical characterizations (S-1), evaluation of photocatalytic activity (S-2), intensity measurements (S-3), degradation kinetic (S-4), recycling and stability test (S-5), evaluation of apparent quantum yield (Q_{app}) and electrical energy per order (E_{EO}) (S-6), detection of reactive species (S-7), electrochemical impedance spectroscopy (EIS) (S-8), and computational methodology (S-9) are stated in supporting information.

Conclusions

To the best of our knowledge, this is the first time we have shown that the fabricating a binary system of S-scheme CuO@TiO₂ heterojunction composite photocatalyst via a simple solid-state reaction is a promising strategy for boosting the photocatalytic degradation of toxic organics. The existence of heterojunction between TiO₂ and CuO was demonstrated by the measurements of catalytic activity, including HRTEM, Raman, XPS, UV-Vis. PL and EIS. Also, the experimental optical results showed that the CuO@TiO₂ reduced the band gap by shifting the band-gap of commercial TiO₂ (3.43 eV) into a new band gap of CuO@TiO₂ (2.35 eV) and DFT calculation explained that by details. The S-scheme CuO@TiO₂ heterojunction composite, displaying the lowest PL intensity, shows the highest activity, and reveals the apparent quantum efficiency of 3.2%. The higher photocatalytic activity was qualified to the well-designed S-scheme CuO@TiO₂ heterojunction, which remarkably aids the separation of photogenerated electrons and holes by the synergistic impacts at the interface of the catalyst components. Further, the most active species in the photodegradation of AR8 dye was detected as ·OH and ·O₂⁻. However, the experimental results demonstrated that the h⁺, and e⁻ are also involved in the degradation process. The plausible degradation mechanism by p-n S-scheme CuO@TiO₂ heterojunction was determined and discussed based upon detection of reactive oxygen species, PL and EIS, which found that the the electron transfer from CuO to TiO₂, followed by hole transfer from TiO₂ to CuO was attributed to be the most likely mode of charge transfer in the S-scheme CuO@TiO₂ system. The recycling experiment revealed that the AR8 dye is diminished by 4.5% after five runs of CuO@TiO₂. The result certified the suitable stability of CuO@TiO₂ for long-term applications. Further theoretical work is currently underway to investigate the formation of S-scheme CuO@TiO₂ heterojunction. Potentially, this study offers a new way for the strategy of the highly efficient S-scheme heterojunction photocatalyst for the effective degradation of organic pollutants in large scales.

Data availability

All data generated or analyzed during this study are included in this article (and its Supplementary Information file).

Received: 7 September 2021; Accepted: 21 January 2022

Published online: 09 February 2022

References

- Hoffmann, M. R., Martin, S. T., Choi, W. & Bahnemann, D. W. Environmental applications of semiconductor photocatalysis. *Chem. Rev.* **95**, 69–96 (1995).
- Hamad, H. A., Sadik, W. A., Abd El-latif, M. M., Kashyout, A. B. & Feteha, M. Y. Photocatalytic parameters and kinetic study for degradation of dichlorophenol-indophenol (DCPIP) dye using highly active mesoporous TiO₂ nanoparticles. *J. Environ. Sci.* **43**, 26–39 (2016).
- Yang, L. *et al.* Photoelectrocatalytic oxidation of bisphenol A over mesh of TiO₂/graphene/Cu₂O. *Appl. Catal. B Environ.* **183**, 75–85 (2016).
- Hamad, H. *et al.* On the interactions and synergism between phases of carbon–phosphorus–titanium composites synthesized from cellulose for the removal of the orange-G dye. *Materials* **11**, 1766 (2018).
- Liu, L. *et al.* In situ loading of ultra-small Cu₂O particles on TiO₂ nanosheets to enhance the visible-light photoactivity. *Nanoscale* **4**, 6351–6359 (2012).
- Wojcieszak, D. *et al.* Investigations of structure and electrical properties of TiO₂/CuO thin film heterostructures. *Thin Solid Films* **690**, 137538 (2019).
- Al-Jawhari, H. A. A review of recent advances in transparent p-type Cu₂O-based thin film transistors. *Mater. Sci. Semicond. Process.* **40**, 241–252 (2015).
- Ibrahim, M. M. *et al.* Direct Z-scheme of Cu₂O/TiO₂ enhanced self-cleaning, antibacterial activity, and UV protection of cotton fiber under sunlight. *Appl. Surf. Sci.* **479**, 953–962 (2019).
- Wang, Y. *et al.* A unique Cu₂O/TiO₂ nanocomposite with enhanced photocatalytic performance under visible light irradiation. *Ceram. Int.* **43**, 4866–4872 (2017).
- Wu, J. *et al.* Photocatalytic oxidation of gas-phase Hg⁰ by carbon spheres supported visible-light-driven CuO–TiO₂. *J. Ind. Eng. Chem.* **46**, 416–425 (2017).
- Xu, F. *et al.* Unique S-scheme heterojunctions in self-assembled TiO₂/CsPbBr₃ hybrids for CO₂ photoreduction. *Nat. Commun.* **11**, 4613 (2020).
- Xu, Q., Zhang, L., Cheng, B., Fan, J. & Yu, J. S-scheme heterojunction photocatalyst. *Chem* **6**, 1543–1559 (2020).
- Arshad, A. *et al.* Solar light triggered catalytic performance of graphene-CuO nanocomposite for waste water treatment. *Ceram. Int.* **43**, 10654–10660 (2017).
- Hamad, H., El-Latif, M. A., Kashyout, A., Sadik, W. & Feteha, M. Optimizing the preparation parameters of mesoporous nanocrystalline titania and its photocatalytic activity in water: Physical properties and growth mechanisms. *Process Saf. Environ. Protect.* **98**, 390–398 (2015).
- Kavirasan, K. *et al.* Photocatalytic and photoelectrocatalytic performance of sonochemically synthesized Cu₂O@TiO₂ heterojunction nanocomposites. *Ultrason. Sonochem.* **51**, 223–229 (2019).
- Shi, Q. *et al.* CuO@TiO₂ heterojunction composites: An efficient photocatalyst for selective oxidation of methanol to methyl formate. *J. Mater. Chem. A* **7**, 2253–2260 (2019).

17. Hamad, H. A., Abd El-latif, M. M., Kashyout, A. B., Sadik, W. A. & Feteha, M. Y. Synthesis and characterization of core-shell-shell magnetic (CoFe₂O₄-SiO₂-TiO₂) nanocomposites and TiO₂ nanoparticles for the evaluation of photocatalytic activity under UV and visible irradiation. *New J. Chem.* **39**, 3116–3128 (2015).
18. Shannon, R. D. Revised effective ionic radii and systematic studies of interatomic distances in halides and chalcogenides. *Acta Cryst.* **A32**, 751–767 (1976).
19. Elsenety, M. M. *et al.* Synthesis, characterization of ((CH₃)₃S)₂SnI_{6-n}Cl_n and ((CH₃)₃S)₂SnI_{6-n}Br_n (n=1, 2) perovskites and use in dye-sensitized solar cells. *Mater. Chem. Phys.* **239**, 122310 (2020).
20. Zedan, A. F., Allam, N. K. & AlQaradawi, S. Y. A study of low-temperature CO oxidation over mesoporous CuO-TiO₂ nanotube catalysts. *Catalysts* **7**, 129–146 (2017).
21. Munawar, Kh. *et al.* Single step fabrication of CuO-MnO₂-TiO₂ composite thin films with improved photoelectrochemical response. *RSC Adv.* **7**, 15885–15893 (2017).
22. Navas, J. *et al.* Experimental and theoretical study of the electronic properties of Cu-doped anatase TiO₂. *Phys. Chem. Chem. Phys.* **16**, 3835–3845 (2014).
23. Segovia-Guzmán, M. O. *et al.* Green Cu₂O/TiO₂ heterojunction for glycerol photoreforming. *Catal. Today* **349**, 88–97 (2020).
24. Deng, C. *et al.* No reduction by CO over CuO supported on CeO₂-Doped TiO₂: The effect of the amount of a few CeO₂. *Phys. Chem. Chem. Phys.* **17**, 16092–16109 (2015).
25. Chen, X. & Mao, S. S. Titanium dioxide nanomaterials: Synthesis, properties, modifications, and applications. *Chem. Rev.* **107**, 2891–2959 (2007).
26. Yan, L., Yang, L., Tao, F. & Luo, X. Highly efficient and stable Cu₂O-TiO₂ intermediate photocatalytic water splitting. *Ceram. Int.* **46**, 9455–9463 (2020).
27. Chen, C. *et al.* Surface defect-engineered silver silicate/ceria p-n heterojunctions with a flower-like structure for boosting visible light photocatalysis with mechanistic insight. *J. Colloid Interface Sci.* **564**, 442–453 (2020).
28. Hamad, H. *et al.* Functionalized cellulose for the controlled synthesis of novel carbon-Ti nanocomposites: physicochemical and photocatalytic properties. *Nanomaterials* **10**, 729 (2020).
29. Zhou, W. *et al.* Enhanced photocatalytic degradation of xylene by blackening TiO₂ nanoparticles with high dispersion of CuO. *J. Hazard. Mater.* **391**, 121642 (2020).
30. Kubiak, A. *et al.* Microwave-assisted synthesis of a TiO₂-CuO heterojunction with enhanced photocatalytic activity against tetracycline. *Appl. Surf. Sci.* **520**, 146344 (2020).
31. Srevarit, W. *et al.* Photoelectrocatalytic H₂ evolution enhancement over CuO-decorated TiO₂ nanocatalysts and promoting *E. coli* degradation. *J. Alloys Compd.* **859**, 157818 (2021).
32. Shan, Z. *et al.* Low-cost nanostructured electrode containing carbon, oxygen, and titanium for efficient oxygen evolution reaction. *J. Am. Chem. Soc.* **137**, 11996–12005 (2015).
33. Ye, D., Wang, X., Liu, H. & Wang, H. Insights into the effects of sulfate species on CuO@TiO₂ catalysts for NH₃-SCR reactions. *Mol. Catal.* **496**, 111191 (2020).
34. Liu, Z. & Zhou, C. Improved photocatalytic activity of nano CuO-incorporated TiO₂ granules prepared by spray drying. *Prog. Nat. Sci. Mater. Int.* **25**, 334–341 (2015).
35. Fang, B., Xing, Y., Bonakdarpour, A., Zhang, S. & Wilkinson, D. P. Hierarchical CuO-TiO₂ hollow microspheres for highly efficient photodriven reduction of CO₂ to CH₄. *ACS Sustain. Chem. Eng.* **3**, 2381–2388 (2015).
36. Ying, L., Xu, Z. G. & Chu, Y. C. Cu₂O nanocrystals/TiO₂ microspheres film on a rotating disk containing long-afterglow phosphor for enhanced round-the-clock photocatalysis. *Appl. Catal. B Environ.* **224**, 239–248 (2018).
37. Hamad, H. *et al.* Synthesis of Ti₃O₅ nanocrystals in mild synthesis conditions for the degradation of pollutants under solar light. *Appl. Catal. B Environ.* **241**, 385–392 (2019).
38. Ali, R. M., Elkatory, M. R. & Hamad, H. A. Highly active and stable magnetically recyclable CuFe₂O₄ as a heterogenous catalyst for efficient conversion of waste frying oil to biodiesel. *Fuel* **268**, 117297 (2020).
39. Shi, Q., Li, Y., Zhan, E., Ta, N. & Shen, W. Anatase TiO₂ hollow nanosheets: dual roles of F⁻, formation mechanism, and thermal stability. *CrystEngComm* **16**, 3431–3437 (2014).
40. Li, B., Hao, Y., Zhang, B., Shao, X. & Hu, L. A multifunctional noble-metal-free catalyst of CuO@TiO₂ hybrid nanofibers. *Appl. Catal. A Gen.* **531**, 1–12 (2017).
41. Reddy, N. L., Emin, S., Kumari, V. D. & Muthukonda, V. S. CuO quantum dots decorated TiO₂ nanocomposite photocatalyst for stable hydrogen generation. *Ind. Eng. Chem. Res.* **57**, 568–577 (2018).
42. Qamar, M. T., Aslam, M., Ismail, I. M. I., Salah, N. & Hameed, A. Synthesis, characterization, and sunlight mediated photocatalytic activity of CuO coated ZnO for the removal of nitrophenols. *ACS Appl. Mater. Interfaces* **7**, 8757–8769 (2015).
43. Bashiri, R., Mohamed, N. M., Kait, C. F. & Sufian, S. Hydrogen production from water photosplitting using Cu/TiO₂ nanoparticles: Effect of hydrolysis rate and reaction medium. *Int. J. Hydrogen Energy* **40**, 6021–6037 (2015).
44. Kong, J., Rui, Z., Liu, S., Liu, H. & Ji, H. Homeostasis in Cu₂O/SrTiO₃ hybrid allows highly active and stable visible light photocatalytic performance. *Chem. Commun.* **53**, 12329–12332 (2017).
45. Meng, A., Zhang, J., Xu, D., Cheng, B. & Yu, J. Enhanced photocatalytic H₂-production activity of anatase TiO₂ nanosheet by selectively depositing dual-cocatalysts on 101 and 001 facets. *Appl. Catal. B* **198**, 286–294 (2016).
46. Zhu, Y. P., Ren, T. Z. & Yuan, Z. Y. Mesoporous phosphorus-doped g-C₃N₄ nanostructured flowers with superior photocatalytic hydrogen evolution performance. *ACS Appl. Mater. Interfaces* **7**, 16850–16856 (2015).
47. Zhang, Y.-H., Liu, M.-M., Chen, J.-L., Xie, K.-F. & Fang, S.-M. Dendritic branching Z-scheme Cu₂O/TiO₂ heterostructure photocatalysts for boosting H₂ production. *J. Phys. Chem. Solids* **152**, 109948 (2021).
48. Elsenety, M. M. *et al.* Stability improvement and performance reproducibility enhancement of perovskite solar cells following (FA/MA/Cs)PbI_{3-x}Br_x/(CH₃)₃SPbI₃ dimensionality engineering. *ACS Appl. Energy Mater.* **3**, 2465–2477 (2020).
49. Yan, L., Yang, F., Tao, Ch. Y., Luo, X. & Zhang, L. Highly efficient and stable Cu₂O-TiO₂ intermediate photocatalytic water splitting. *Ceram. Int.* **46**, 9455–9463 (2020).
50. Motawea, M. M. *et al.* Mesoporous hierarchical ZrO₂@rice straw-derived SiO₂ nanocomposite for rapid adsorption and sunlight-driven photocatalytic degradation of methylene blue. *Photochem. Photobiol. A Chem.* **426**, 113758 (2022).
51. Mekkey, S. D., Sultan, M. E., Elsenety, M. M., Helal, A. & Elsayed, B. A. Photocatalytic degradation of rhodamine B in the visible region using nanostructured CoAl_{2-x}La_xO₄ (x = 0, 001, 003, 007, and 009) series: Photocatalytic activity and DFT calculations. *Inorg. Chem. Commun.* **136**, 109176 (2022).
52. Elsenety, M. M., Elsayed, B. A., Ibrahim, A. I. & Bedair, M. A. Photophysical, DFT and molecular docking studies of Sm(III) and Eu(III) complexes of newly synthesized coumarin ligand. *Inorg. Chem. Commun.* **121**, 108213 (2020).
53. Lu, Y. *et al.* Cu₂O nanocrystals/TiO₂ microspheres film on a rotating disk containing long-afterglow phosphor for enhanced round-the-clock photocatalysis. *Appl. Catal. B Environ.* **224**, 239–248 (2018).
54. Zeleke, O. A. & Kuo, D.-H. A two-oxide nanodiode system made of double-layered p-type Ag₂O@n-type TiO₂ for rapid reduction of 4-nitrophenol. *Phys. Chem. Chem. Phys.* **18**, 4405–4414 (2016).
55. Lam, S.-M., Sin, J.-C., Abdullah, A. Z. & Mohamed, A. R. Photocatalytic degradation of resorcinol, an endocrine disrupter, by TiO₂ and ZnO suspensions. *Environ. Technol.* **34**, 1097–1106 (2013).

56. Sadik, W. A., El-Demerdash, A. M., Nashed, A. W., Mostafa, A. A. & Hamad, H. A. Highly efficient photocatalytic performance of Cu₂O@TiO₂ nanocomposite: Influence of various inorganic oxidants and inorganic anions. *J. Mater. Res. Technol.* **8**, 5405–5414 (2019).
57. Bi, Q., Gao, Y., Dang, Ch., Wang, Z. & Xue, J. Study on the photoelectrocatalytic performance of a WO₃ thin film electrode by constructing a BiOI/WO₃ heterojunction. *CrystEngComm* **21**, 6744–6757 (2019).
58. Shokry, H., Elkady, M. & Hamad, H. Nano activated carbon from industrial mine coal as adsorbents for removal of dye from simulated textile wastewater: Operational parameters and mechanism study. *J. Mater. Res. Technol.* **8**, 4477–4488 (2019).
59. Wu, Y. *et al.* Constructing NiFe-LDH wrapped Cu₂O nanocube heterostructure photocatalysts for enhanced photocatalytic dye degradation and CO₂ reduction via Z-scheme mechanism. *J. Alloys Compd.* **831**, 154723 (2020).
60. Zhang, T. *et al.* Effect of Cu doping on the SCR activity over the Cu_mCe_{0.1-m}TiO_x (m = 0.01, 0.02 and 0.03) catalysts. *Appl. Catal. A Gen.* **570**, 251–261 (2019).
61. Pal, J., Sasmal, A. K., Ganguly, M. & Pal, T. Surface plasmon effect of Cu and presence of n–p heterojunction in oxide nanocomposites for visible light photocatalysis. *J. Phys. Chem. C* **119**, 3780–3790 (2015).
62. Trang, T. N. Q. *et al.* A high-efficiency photoelectrochemistry of Cu₂O/TiO₂ nanotubes based composite for hydrogen evolution under sunlight. *Compos. B Eng.* **174**, 106969 (2019).
63. Cheng, C. *et al.* An inorganic/organic S-scheme heterojunction H₂-production photocatalyst and its charge transfer mechanism. *Adv. Mater.* **33**, 2100317 (2021).
64. Wang, L., Cheng, B., Zhang, L. & Yu, J. In situ irradiated XPS investigation on S-scheme TiO₂@ZnIn₂S₄ photocatalyst for efficient photocatalytic CO₂ reduction. *Small* **17**, 2103447 (2021).
65. Meng, A. *et al.* TiO₂/polydopamine S-scheme heterojunction photocatalyst with enhanced CO₂-reduction selectivity. *Appl. Catal. B Environ.* **289**, 120039 (2021).
66. He, F., Meng, A., Cheng, B., Ho, W. & Yu, J. Enhanced photocatalytic H₂-production activity of WO₃/TiO₂ step-scheme heterojunction by graphene modification. *Chin. J. Catal.* **41**, 9–20 (2020).
67. Geng, Z. *et al.* Incorporation of Cu₂O nanocrystals into TiO₂ photonic crystal for enhanced UV–visible light driven photocatalysis. *J. Alloy. Compd.* **644**, 734–741 (2015).
68. Bai, X., Ma, L., Dai, Z. & Shi, H. Electrochemical synthesis of p-Cu₂O/n-TiO₂ heterojunction electrode with enhanced photoelectrocatalytic activity. *Mater. Sci. Semicond. Proc.* **74**, 319–328 (2018).
69. Xi, Z., Li, C., Zhang, L., Xing, M. & Zhang, J. Synergistic effect of Cu₂O/TiO₂ heterostructure nanoparticle and its high H₂ evolution activity. *Int. J. Hydrog. Energy* **39**, 6345–6353 (2014).

Acknowledgements

The authors are deeply grateful to both the City of Scientific Research and Technological Applications (SRTA-City) and Alexandria University in Egypt for supporting and facilitating this study. H. Hamad also acknowledges the Faculty of Science, Warsaw University for the computer services.

Author contributions

H.H.: Conceptualization, methodology, investigation, software, validation, formal analysis, visualization, data curation, funding acquisition, writing—original draft, writing—reviewing & editing, resources, supervision, project administration. M.E.: Formal analysis, visualization, data curation, writing—reviewing & editing; W.S.: Methodology, investigation, formal analysis; A.-G.E.-D.: Investigation; A.N.: Investigation; A.M.: Methodology, investigation, formal analysis; S.E.: Methodology, investigation, validation, formal analysis, funding acquisition.

Competing interests

The authors declare no competing interests.

Additional information

Supplementary Information The online version contains supplementary material available at <https://doi.org/10.1038/s41598-022-05981-7>.

Correspondence and requests for materials should be addressed to H.H.

Reprints and permissions information is available at www.nature.com/reprints.

Publisher's note Springer Nature remains neutral with regard to jurisdictional claims in published maps and institutional affiliations.



Open Access This article is licensed under a Creative Commons Attribution 4.0 International License, which permits use, sharing, adaptation, distribution and reproduction in any medium or format, as long as you give appropriate credit to the original author(s) and the source, provide a link to the Creative Commons licence, and indicate if changes were made. The images or other third party material in this article are included in the article's Creative Commons licence, unless indicated otherwise in a credit line to the material. If material is not included in the article's Creative Commons licence and your intended use is not permitted by statutory regulation or exceeds the permitted use, you will need to obtain permission directly from the copyright holder. To view a copy of this licence, visit <http://creativecommons.org/licenses/by/4.0/>.

© The Author(s) 2022